Electronic Research Archive

http://www.aimspress.com/journal/era

ERA, 33(10): 6070–6095.
DOI: 10.3934/era.2025270
Received: 16 August 2025
Revised: 09 October 2025
Accepted: 14 October 2025
Published: 17 October 2025

Research article

The effect of the feedback inhibition of heterogeneous external globus pallidus on beta oscillations in an extended basal ganglia network

Zihan Li[1], **Xia Shi**[2,3,*] **and Bei Bai**[2]

[1] School of Electronic Engineering, Beijing University of Posts and Telecommunications, Beijing 100876, China

[2] School of Mathematical Sciences, Beijing University of Posts and Telecommunications, Beijing 100876, China

[3] Key Laboratory of Mathematics and Information Networks (Beijing University of Posts and Telecommunications), Ministry of Education, Beijing 100876, China

* **Correspondence:** Email: shixiabupt@163.com.

Abstract: Pathological β-band oscillations (13–35 Hz) in the basal ganglia (BG) are strongly associated with Parkinson's disease (PD). Recent evidence shows that subpopulations of external globus pallidus (GPe) neurons exhibit distinct responses to pathological conditions, and that their inhibitory feedback to the striatum strongly shape BG dynamics, features often overlooked in conventional models. To address this, we developed an extended BG network using a modified Hodgkin–Huxley framework, incorporating two GPe subclasses, arkypallidal (TA) and prototypical (TI), along with striatal medium spiny neurons (MSNs) and fast-spiking interneurons (FSIs). Simulations revealed that mutual inhibition within the GPe drives TI neurons from tonic firing into β-bursting, retrogradely suppressing striatal activity through the GPe–FSI–MSN loop and disrupting direct/indirect pathway balance. We further show that GPe-TA projections exert strong inhibitory control over striatal populations, and that reducing MSN M-current reproduces β oscillations that propagate downstream. Blocking D2 MSN $\rightarrow$ GPe-TI and GPe-TI $\rightarrow$ GPe-TA synapses restores normal TI firing. Our results emphasize the role of GPe heterogeneity in pathological oscillations and suggest circuit-level therapeutic strategies for PD.

Keywords: heterogeneous GPe; Bursting; β-band oscillations; Parkinson's disease; basal ganglia

1. Introduction

The basal ganglia (BG) are subcortical nuclei located beneath the cerebral cortex and participate in diverse processes that extend beyond motor regulation, encompassing a variety of neural functions.

Among these, they are critically involved in the pathology of Parkinson's disease (PD). PD is widely recognized as a long-term degenerative disorder of the nervous system, primarily arising from the progressive depletion of dopamine-producing neurons in the midbrain. This dopaminergic loss disrupts the functional organization of the BG, thalamus (TC), and cortex [1–5]. A prominent electrophysiological signature of PD is the emergence of excessive β-band oscillations (13–35 Hz), which appear as pathological synchronization within the BG. Conventional BG models emphasize three main circuits: direct, indirect, and hyperdirect pathways [6]. Within this framework, the external globus pallidus (GPe) is recognized as a key structure of the indirect pathway, where it plays a major role in modulating the spread of abnormal oscillatory activity [7, 8]. Experimental observations, including those by Corbit and colleagues, demonstrated that feedback inhibition conveyed by GPe neurons to the striatum can intensify synchronous activity and oscillatory patterns in PD states [9]. More recently, research attention has increasingly shifted toward elucidating the contribution of the GPe to the persistence of pathological β oscillations [10, 11]. Physiological studies further suggest that distinct GPe subpopulations undergo heterogeneous alterations in disease conditions, underscoring the complexity that classical models fail to capture. Consequently, there is a pressing need for advanced computational approaches capable of representing the intricate function of the GPe in BG circuitry.

In recent years, investigations into the heterogeneity of the GPe have expanded markedly. The earliest scheme for classifying GPe neurons was introduced by Delong through behavioral studies in primates [12]. Later, Albin et al. refined this by distinguishing high-frequency paused (HFP) neurons and low-frequency burst (LFB) neurons, classified on the basis of their intrinsic firing properties [13]. Building on these observations, Mallet proposed two principal subclasses based on contrasting firing properties: Type A neurons (GPe-TA, arkypallidal) and Type I neurons (GPe-TI, prototypic) [14]. Further physiological evidence using molecular markers confirmed that GPe neurons exhibit wide heterogeneity in both electrophysiological and synaptic features [15]. Abecassis later provided a visual framework using a three-layer concentric chart to illustrate marker distribution and the relative proportions of these subclasses [16]. Since marker-based classifications often overlap and their projection patterns are not fully delineated, we adopt Mallet's dichotomy of GPe-TA and GPe-TI. GPe-TI neurons constitute about 75% of the population, maintain continuous activity, and project broadly to the substantia nigra pars reticulata (SNR) and the subthalamic nucleus (STN) [9,15,17,18]. In contrast, GPe-TA neurons make up roughly 25% and send their projections mainly to the striatum [15, 18]. Although GPe-TA neurons provide substantial inhibitory input to the striatum, their computational role has been less explored. To address this gap, we develop a model that explicitly incorporates this inhibitory pathway to investigate its influence on striatal network dynamics.

We develop a computational model of the BG, illustrated in Figure 1, which incorporates the striatum, GPe, STN, and GPi. Within the striatum, the primary neuronal populations consist of medium spiny neurons (MSNs) and fast-spiking interneurons (FSIs). MSNs are further subdivided into D1-type and D2-type cells. The direct pathway, driven by D1 receptor–positive MSNs (D1 MSNs), promotes motor actions [19], in contrast to the indirect pathway, mediated by D2 receptor–positive MSNs (D2 MSNs), which suppresses movement [20, 21]. The interplay between these two pathways ensures balanced striatal output, thereby exerting a profound impact on GPe dynamics. By modulating striatal projections, the model captures how changes in coupling affect network behavior. Physiologically grounded parameter settings are adopted to replicate the healthy state in simulations. Interactions among heterogeneous GPe subpopulations are shown to be essential for shaping β oscillations and

influencing striatal responses. Our simulations reveal that β oscillations induced by reduced M-current conductance in MSNs, together with inhibitory inputs from the GPe, propagate through the indirect pathway to GPe-TI neurons. Combined with direct-pathway modulation of MSN activity, this mechanism reproduces pathological oscillatory states within the BG. We further tested which synaptic disconnections are sufficient to restore normal activity in GPe-TI neurons. Overall, the results emphasize the joint importance of neuronal intrinsic properties and synaptic connectivity, while also suggesting potential therapeutic approaches for reestablishing healthy dynamics. Through this framework, a clearer understanding of the mechanisms involved in Parkinson's disease is achieved, along with indications for strategies that may regulate its progression.

2. Materials and methods

2.1. The network model

The constructed network includes several distinct neuronal groups, namely D1 MSNs, D2 MSNs, FSIs, STN, GPe-TA, GPe-TI, GPi, and TC neurons, all modeled as point neurons (see Figure 1; following [14]). Building upon a previously established framework [22], which originally considered only the STN, GPe, GPi, and TC circuits, the present work extends the model by integrating the striatal ensemble composed of D1 MSNs, D2 MSNs, and FSIs together with GPe-TA and GPe-TI populations [14]. For reproducibility, the connectivity is also provided as an adjacency matrix in Figure A1.

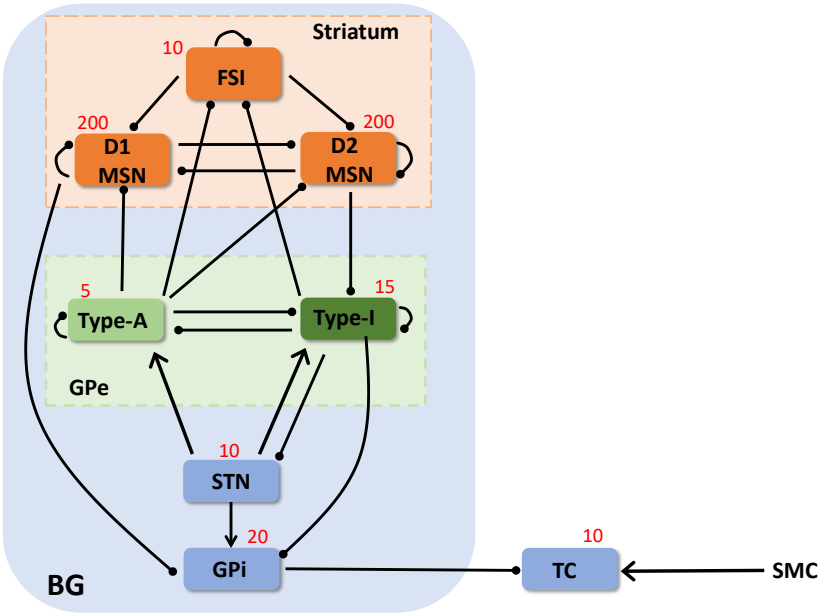

Figure 1. Illustration of the extended BG-TC network layout, showing the interconnections among STN, GPi, D1/D2 MSNs, FSIs, TC, sensorimotor cortex (SMC), and GPe-TA/TI neurons. Lines ending with circles denote inhibition; arrowheads denote excitation. Red numbers indicate neuron counts.

Grounded in biological experimental findings, we adjusted the neuron quantities within the

extended BG network model to more closely align with the experimental data regarding neuronal firing characteristics. Dunedin assessed the overall neuronal counts in six regions of the rat basal ganglia by applying stereological counting strategies combined with systematic random sampling. Subsequently, the counts for TC, STN, GPe, GPi, SNr, and striatum were determined [23]. Gittis et al. measured the number of FSIs, D1 MSNs, and D2 MSNs using the optical disector method, identifying 10, 200, and 200 cells, respectively [24]. Abdi and colleagues reported that, in rats, GPe-TA (arkypallidal) neurons account for about 25% of the population, whereas GPe-TI (prototypical) neurons make up the remaining 75%. These estimates were obtained through combined anatomical and electrophysiological analyses [17]. By synthesizing the findings from these studies and adhering to the rules of proportionality and forensics, we hypothesize in our extended BG model that the STN has 10 neurons, GPe-TI has 15 neurons, GPe-TA has 5 neurons, GPi has 20 neurons, FSI includes 10 neurons, D1 MSN encompasses 200 neurons, and D2 MSN has 200 neurons.

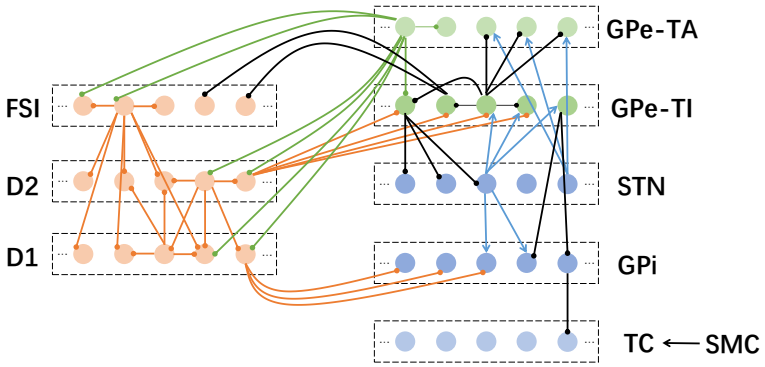

Figure 2. Connectivity diagram of the extended BG-TC network model, incorporating FSI, D1, D2, STN, TA, TI, GPi, and TC nuclei. Excitatory links are illustrated with arrows, whereas inhibitory links are indicated by lines terminating in circles. Each FSI neuron targets three nearby D1 MSNs, three D2 MSNs, and provides inhibition to two additional FSIs. D1 MSNs inhibit two neighboring D2 MSNs, two D1 MSNs, and three GPi neurons. D2 MSNs inhibit three D1 MSNs, four TI neurons, and two D2 MSNs. Each STN neuron projects to two GPi neurons as well as three TA and TI neurons. TI neurons deliver inhibition to three STN neurons, three TA neurons, three TI neurons, two FSIs, and two GPi neurons. TA neurons inhibit two D1 MSNs, two D2 MSNs, two FSIs, one TI, and one TA neuron. Rounding out the model, each GPi neuron imparts an inhibitory signal to one TC neuron, and each TC neuron not only receives one such inhibitory projection from a GPi neuron, but also taps into information streaming from the sensorimotor SMC. The corresponding adjacency matrix is provided in Figure A1.

Drawing inspiration from the sparse connection framework proposed by So et al. [22], we incorporated a similar connectivity principle in the extended BG network. Figure 2 illustrates that each FSI neuron targets three nearby D1 MSNs and three D2 MSNs, while also providing inhibition to two other FSIs [25,26]. According to projection probabilities reported in earlier computational models [27],

D1 MSNs were modeled to suppress two neighboring D2 MSNs, two nearby D1 MSNs, and three GPi neurons. D2 MSNs, in turn, inhibit two D2 MSNs, three D1 MSNs, and four adjacent GPe-TI neurons. GPe-TI neurons deliver inhibitory signals to three GPe-TI neurons, three GPe-TA neurons, two FSIs, and two GPi neurons [28–31]. Based on evidence of heterogeneous GPe connectivity [18, 28, 32], each GPe-TA neuron was assumed to inhibit one GPe-TA, one GPe-TI, and two cells from each of the following: D1 MSNs, D2 MSNs, and FSIs. Furthermore, STN neurons provide excitatory inputs to three GPe-TI neurons, three GPe-TA neurons, and two GPi neurons. Although experimental data indicate differences in the detailed connectivity between STN and heterogeneous GPe neurons [18,32], these projections were simplified in our implementation, with the variations in synaptic efficacy captured by their conductance densities. Following the design in So et al. [22], the network was arranged in a ring-like structure, ensuring that the first and last neurons within each population were treated as neighbors. This circular organization preserves connectivity across nuclei even when their cell numbers differ in the extended BG model.

2.2. Model for each neuron type

In this work, the neuronal dynamics of GPe, GPi, STN, and TC cells are represented using a Hodgkin–Huxley (HH) type formulation, following the structure proposed by So et al. [22] with appropriate modifications. The models incorporate a set of ionic currents, namely the leakage current I_L, sodium current I_{Na}, potassium current I_K, T-type low-threshold Ca^{2+} current I_T, high-threshold Ca^{2+} current I_{Ca}, and the Ca^{2+}-activated after-hyperpolarization current I_{AHP}. The membrane potential dynamics of the TC, STN, and GPi neurons are described as follows:

$$C_m \frac{dv_{TC}}{dt} = -I_{Na} - I_K - I_L - I_T - I_{GPi\to TC} - I_{SMC}, \tag{2.1}$$

$$C_m \frac{dv_{STN}}{dt} = -I_{Na} - I_K - I_L - I_T - I_{Ca} - I_{AHP} - I_{TI\to STN} + I_{STNapp}, \tag{2.2}$$

$$C_m \frac{dv_{GPi}}{dt} = -I_{Na} - I_K - I_L - I_T - I_{Ca} - I_{AHP} - I_{STN\to GPi} - I_{TI\to GPi} - I_{D1\to GPi} + I_{GPiapp}, \tag{2.3}$$

where $C_\mathrm{m} = 1\mu\,\mathrm{F/cm^2}$ represents the membrane capacitance and I_{SMC} is the signal received from the cortical sensorimotor input, which is modeled as a series of random monophasic current pulses. I_{app} is the applied constant current. Here, $I_{STNapp} = 33\,\mu\mathrm{A/cm^2}$ and $I_{GPiapp} = 22\,\mu\mathrm{A/cm^2}$ are to keep the model in a controlled state. All specific formulas and related parameters for these neurons can be found in [22].

For the MSN model, the ionic components consist of the sodium current I_{Na}, potassium current I_K, leak current I_L, M-current I_M, inward-rectifying potassium current I_{Kir}, and synaptic inputs [33]. For D1 MSNs, synaptic inputs include inhibitory projections from D2 MSNs, other D1 MSNs, FSIs, and GPe-TA neurons, i.e., $I_{D2\to D1}, I_{D1\to D1}, I_{FSI\to D1}$, and $I_{TA\to D1}$. For D2 MSNs, inhibitory synaptic currents originate from D1 MSNs, D2 MSNs, FSIs, and GPe-TA neurons, i.e., $I_{D1\to D2}, I_{D2\to D2}, I_{FSI\to D2}$, and $I_{TA\to D2}$. The external inputs are represented by $I_{D1app} = 3.05\,\mu\mathrm{A/cm^2}$ and $I_{D2app} = 2.85\,\mu\mathrm{A/cm^2}$ [33].

The membrane potential of MSNs is governed by the following equations:

$$C_m \frac{dv_{D1MSN}}{dt} = -I_{Na} - I_K - I_L - I_M - I_{Kir} - I_{D2\to D1} - I_{D1\to D1} - I_{TA\to D1} - I_{FSI\to D1} + I_{D1app}, \tag{2.4}$$

$$C_m \frac{dv_{D2MSN}}{dt} = -I_{Na} - I_K - I_L - I_M - I_{Kir} - I_{D1\to D2} - I_{D2\to D2} - I_{TA\to D2} - I_{FSI\to D2} + I_{D2app}, \quad (2.5)$$

where $C_m = 1\mu\text{F/cm}^2$ denotes the membrane capacitance. Constant synaptic conductance g, together with the reversal potential E of each current, and the gating variables m, n, M (activation), and h (inactivation) for MSNs and FSIs, follow the equations summarized in Tables 1 and 2 [33]. The gating variables m, n, M, and h evolve as

$$\frac{dx}{dt} = \frac{x_\infty - x}{\tau_x}, \quad x \in \{m, h, n, M\}, \quad (2.6)$$

with x_∞ representing the steady-state value and τ_x the time constant of decay:

$$x_\infty = \frac{\alpha_x}{\alpha_x + \beta_x}, \qquad \tau_x = \frac{1}{\alpha_x + \beta_x}. \quad (2.7)$$

Table 1. Equations and parameter values used in the MSN cell model.

Current	Equation	Gating Variables α	Gating Variables β	Parameters
I_{Na}	$g_{Na}m^3h(V - E_{Na})$	$\alpha_m = \frac{0.32(V+54)}{1-\exp(-(V+54)/4)}$ $\alpha_h = 0.128\exp(-(V+50)/18)$	$\beta_m = \frac{0.28(V+27)}{\exp((V+27)/5)-1}$ $\beta_h = \frac{4}{1+\exp(-(V+27)/5)}$	$g_{Na} = 100\,mS/cm^2$ $E_{Na} = 50\,mV$
I_K	$g_K n^4(V - E_K)$	$\alpha_n = \frac{0.032(V+52)}{1-\exp(-(V+52)/5)}$	$\beta_n = 0.5\exp(-(V+57)/40)$	$g_K = 80\,mS/cm^2$ $E_K = -100\,mV$
I_L	$g_L(V - E_L)$	–	–	$g_L = 0.1\,mS/cm^2$ $E_L = -67\,mV$
I_M	$g_M M(V - E_M)$	$\alpha_M = Q \cdot 10^{-4} \cdot \frac{(V+30)}{1-\exp(-(V+30)/9)}$	$\beta_M = Q \cdot 10^{-4} \cdot \frac{(V+30)}{1-\exp(-(V+30)/9)}$	$g_M = 2\,mS/cm^2$ $E_M = 50\,mV$ $Q = 3.209$
I_{Kir}	$g_{Kir}\alpha_\infty(V - E_{Kir})$	$\alpha_\infty = \frac{1}{1+\exp((V+102)/13)}$	–	$g_{Kir} = 0.175\,mS/cm^2$ (D1) $g_{Kir} = 0.14\,mS/cm^2$ (D2) $E_{Kir} = -82\,mV$

Table 2. Equations and parameter values used in the FSI cell model.

Current	Equation	Gating Variables α	Gating Variables β	Parameters
I_{Na}	$g_{Na}m^3h(V - E_{Na})$	$\alpha_m = \frac{40(75-V)}{\exp(\frac{75-V}{13.5})-1}$ $\alpha_h = 0.0035\exp\left(-\frac{V}{24.186}\right)$	$\beta_m = 1.2262\exp\left(-\frac{V}{42.248}\right)$ $\beta_h = \frac{0.017(-V-51.25)}{\exp(-\frac{V+51.25}{5.2})-1}$	$g_{Na} = 100\,mS/cm^2$ $E_{Na} = 50\,mV$
I_K	$g_K n^4(V - E_K)$	$\alpha_n = \frac{95-V}{\exp(\frac{95-V}{11.8})-1}$	$\beta_n = 0.025\exp\left(-\frac{V}{22.22}\right)$	$g_K = 80\,mS/cm^2$ $E_K = -100\,mV$
I_L	$g_L(V - E_L)$	–	–	$g_L = 0.1\,mS/cm^2$ $E_L = -67\,mV$
I_{gap}	$g_{gap}(V - V_{pre})$	–	–	$g_{\text{gap}} = 0.05\text{mS/cm}^2$ $V_{\text{pre}} = -70\,\text{mV}$

Q = 3.209 denotes the temperature effect, with details provided in Table 1 [33]. For the Kir current, earlier experiments reported an approximate 25% increase in the conductance of D1 MSNs, while no

alteration was found in D2 MSNs [34]. Based on these findings, we assigned $g_{kir} = 0.175\,\mathrm{mS/cm^2}$ for D1 MSNs and $g_{kir} = 0.14\,\mathrm{mS/cm^2}$ for D2 MSNs, with the reversal potential fixed at $E_{kir} = -82\,\mathrm{mV}$ [35]. The corresponding steady-state activation function $a_{\infty(V)}$ is listed in Table 1.

The FSI receives external excitatory inputs and inhibitory projections from the GPe [18, 30, 33, 36, 37]. These interneurons are essential for modulating MSN firing, thereby helping to preserve the functional balance between the direct and indirect pathways. The voltage dynamics of FSIs are formulated as:

$$C_m \frac{dv_{FSI}}{dt} = -I_{Na} - I_K - I_L - I_{FSI\to FSI} - I_{TA\to FSI} - I_{TI\to FSI} - I_{gap} + I_{FSIapp}. \tag{2.8}$$

where $C_m = 1\mu\mathrm{F/cm^2}$. In this expression, $I_{TA\to FSI}$ and $I_{TI\to FSI}$ indicate inhibitory currents originating from GPe-TA and GPe-TI neurons, respectively, while $I_{FSI\to FSI}$ corresponds to recurrent interactions among FSIs. The term I_{gap} accounts for electrical coupling through gap junctions:

$$I_{gap} = g_{gap}(V - V_{pre}), \tag{2.9}$$

with g_{gap} denoting coupling conductance and V_{pre} the presynaptic potential [38]. Comprehensive parameter values for FSIs are available in [33, 38].

The firing characteristics of GPe-TI and GPe-TA neurons, together with their distinct connection patterns to other nuclei, suggest that they may differ in their intrinsic properties [39]. Nevertheless, current studies have not yet clarified the precise ionic channel distinctions between these two GPe subtypes [28, 40]. Experimental evidence has revealed notable differences in firing frequency and action potential (AP) duration across heterogeneous GPe neurons [32, 41]. The duration of action potentials (APs) is largely determined by the conductance density of Na^+ and K^+ channels [42]. To account for the physiological heterogeneity of GPe neurons, the model introduces distinct conductance densities. Previous modeling studies adjusted these conductance parameters for Na^+ and K^+ to reproduce the statistical profiles of firing patterns, thereby providing a refined representation of the two GPe subtypes [43]. In this work, we modify the conductance densities for Na^+ and K^+ in the GPe-TA neuron model so that it more closely matches physiological observations. In our extended model, ionic channel types are the same across heterogeneous GPe neurons, with differences manifested only in Na^+/K^+ conductances and synaptic inputs. The membrane dynamics of the two GPe subpopulations are given by:

$$C_m \frac{dv_{TI}}{dt} = -I_{Na} - I_K - I_L - I_T - I_{Ca} - I_{AHP} - I_{STN\to TI} - I_{TI\to TI} - I_{TA\to TI} - I_{D2\to TI} + I_{TIapp}, \tag{2.10}$$

$$C_m \frac{dv_{TA}}{dt} = -I_{Na} - I_K - I_L - I_T - I_{Ca} - I_{AHP} - I_{STN\to TA} - I_{TI\to TA} - I_{TA\to TA} + I_{TAapp}, \tag{2.11}$$

where $C_m = 1\mu\mathrm{F/cm^2}$. A comprehensive overview of GPe neurons, including ionic currents, and activation and inactivation gating variables is provided in Table 3. This table summarizes not only the variability of ionic currents that are critical for understanding the electrophysiological properties of GPe neurons, but also highlights the gating variables governing neuronal excitation and inhibition. Together, these elements give a more integrated perspective of neuronal dynamics, which is essential for explaining the mechanisms underlying GPe activity.

Table 3. Equations and parameter values used in the GPe cell model.

Current	Equation	Gating Variables α	Gating Variables β	Parameters
I_L	$g_L(V - E_L)$	–	–	$g_L = 0.1\,mS/cm^2$ $E_L = -65\,mV$
I_{Na}	$g_{Na}m_\infty^3 h(V - E_{Na})$	$m_\infty = \frac{1}{1+\exp\left(-\frac{V+37}{10}\right)}$	$h_\infty = \frac{1}{1+\exp\left(-\frac{V+58}{12}\right)}$ $\tau_h = 0.05 + \frac{0.27}{1+\exp\left(-\frac{V+40}{-12}\right)}$	$g_{Na} = 120\,mS/cm^2$ (TI) $g_{Na} = 82.7\,mS/cm^2$ (TA) $E_{Na} = 55\,mV$
I_K	$g_K n^4(V - E_K)$	$n_\infty = \frac{1}{1+\exp\left(-\frac{V+50}{14}\right)}$ $\tau_n = 0.05 + \frac{0.27}{1+\exp\left(-\frac{V+40}{-26}\right)}$	–	$g_K = 30\,mS/cm^2$ (TI) $g_K = 20\,mS/cm^2$ (TA) $E_K = -80\,mV$
I_T	$g_T a_\infty^3 r(V - E_T)$	$a_\infty = \frac{1}{1+\exp\left(-\frac{V+57}{2}\right)}$	$r_\infty = \frac{1}{1+\exp\left(-\frac{V+70}{2}\right)}$	$g_T = 0.5\,mS/cm^2$ $E_T = 0\,mV$
I_{Ca}	$g_{Ca}s_\infty^3(V - E_{Ca})$	$s_\infty = \frac{1}{1+\exp\left(-\frac{V+35}{2}\right)}$	–	$g_{Ca} = 0.15\,mS/cm^2$ $E_{Ca} = 120\,mV$
I_{AHP}	$g_{AHP}(V - E_{AHP})$ $\cdot\left(\frac{[Ca]}{[Ca]+10}\right)$	$[Ca]' = 10^{-4}\left(-I_{Ca} - I_T - 15\cdot[Ca]\right)$	–	$g_{AHP} = 10\,mS/cm^2$ $E_{AHP} = -80\,mV$

Experimental evidence indicates that TI neurons generally fire at higher rates than TA neurons [14]. To reproduce this feature in the model, the applied current for GPe-TI was set greater than that for GPe-TA. Accordingly, the constant input currents were chosen as $I_{TIapp} = 30\,\mu\text{A/cm}^2$ and $I_{TAapp} = 20\,\mu\text{A/cm}^2$. Furthermore, as noted previously, the Na^+ and K^+ conductance densities in TA neurons are reduced compared to those in GPe-TI neurons. In this work, the values were assigned as $g_{Na} = 82.7\,\text{mS/cm}^2$ and $g_K = 20\,\text{mS/cm}^2$. The detailed equations and parameter specifications for GPe neurons are provided in [22].

2.3. Synaptic models

Following the formulation in [22], the synaptic current between a presynaptic neuron a and a postsynaptic neuron b can be written as

$$I_{a\to b} = g_{a\to b}\,(V_b - V_{a\to b})\sum_j S_a^j, \tag{2.12}$$

where $g_{a\to b}$ specifies the peak synaptic conductance and $V_{a\to b}$ denotes the reversal potential of the synapse. The term $\sum_j S_a^j$ accounts for the aggregate contribution of all presynaptic neurons, with S_a^j corresponding to the activity from the jth input.

For STN and GPi, the evolution of synaptic variables is governed by a second-order differential system designed to reflect rapid synaptic dynamics [22]:

$$\begin{aligned} \frac{dS_a^j}{dt} &= z, \\ \frac{dz}{dt} &= 0.0234u(t) - 0.4z - 0.04S_a^j, \end{aligned} \tag{2.13}$$

with $u(t)$ defined as 1 whenever the presynaptic potential crosses the threshold of -10 mV at time t, signifying an action potential; otherwise $u(t) = 0$.

For all remaining synaptic projections, the synaptic variable $S_{k\to j}$ follows the first-order differential form [44]:

$$\frac{\mathrm{d}S_{k\to j}}{\mathrm{d}t} = \alpha\left(1 - S_{k\to j}\right)H_\infty\left(V_k - \theta_g\right) - \beta S_{k\to j}, \tag{2.14}$$

where V_k is the presynaptic membrane potential, α and β are the opening and closing rates of channels, respectively, and H_∞ is given by

$$H_\infty(V) = 1/\left(1 + \exp\left[-\left(V - \theta_g^H\right)/\sigma_g^H\right]\right). \tag{2.15}$$

The synaptic strength from D1 to D2 neurons is weaker compared to that from D2 to D1, while the connection parameters from FSIs to D1 neurons exceed those from FSIs to D2 [45]. Additionally, the STN shows a preference for activating TI neurons [46]. Within the heterogeneous GPe, the average number of axonal boutons is about 500 for TI neurons and 120 for TA neurons, indicating that inhibitory input from TI to TA is considerably stronger than the reverse. Based on this observation, it is reasonable to assume that TI neurons provide the predominant inhibitory input to TA neurons, given that the number of TI-derived synapses far exceeds those originating from TA. Accordingly, in the modeling framework, we incorporate a hierarchical relationship of connection strengths: the inhibitory weight from TI to TI neurons ($g_{TI\to TI}$) is taken to be equal to or stronger than that from TI to TA neurons ($g_{TI\to TA}$), which is in turn not weaker than the strength from TA to TI neurons ($g_{TA\to TI}$). Finally, the connection from TA to TA neurons ($g_{TA\to TA}$) is the weakest among them. Other synaptic parameters in the network are summarized in Table 4, reflecting this hierarchy. In this study, we used synaptic current parameters reported by So et al. [22] for the baseline BG-TC framework, while striatal settings follow prior studies [45]. The system dynamics were integrated with the forward Euler method, employing a time step of 0.01 ms.

Table 4. Synaptic parameters used in the model.

Connection	Value (mS/cm^2)	Connection	Value (mS/cm^2)
$g_{D1\to D2}$	0.15	$g_{D2\to D1}$	0.2
$g_{D1\to D1}$	0.24	$g_{D2\to D2}$	0.23
$g_{FSI\to D1}$	0.14	$g_{FSI\to D2}$	0.12
$g_{FSI\to FSI}$	0.1	$g_{D1\to GPi}$	0.1
$g_{STN\to TA}$	0.15	$g_{STN\to TI}$	0.3
$g_{TI\to GPi}$	1	$g_{D2\to TI}$	0.1
$g_{TA\to D1}$	0.11	$g_{TA\to D2}$	0.15
$g_{TA\to FSI}$	0.16	$g_{TI\to FSI}$	1
$g_{TI\to TI}$	1	$g_{TI\to TA}$	1.2
$g_{TA\to TI}$	0.2	$g_{TA\to TA}$	1

3. Results

3.1. Electrophysiological properties of the extended BG network

To assess the validity of the extended BG model, we compared the firing patterns of interconnected neuronal populations with available experimental observations. Within this framework, GPe-TI neurons correspond to the GPe population in traditional models, while GPe-TA neurons function as an inhibitory projection to the striatum.

Figure 3 illustrates neuronal firing patterns obtained in the healthy state. In the first row, the responses of single STN and GPi neurons reproduce the dynamics described in the computational framework of So et al. [22]. The second and third rows highlight the spiking behavior of MSNs within the striatal circuit and of GPe populations in their recurrent network. Consistent with physiological recordings, D2 MSNs fire at nearly twice the frequency observed in D1 MSNs. The fourth row displays the discharge activity of FSIs, further confirming that the simulated results remain aligned with experimental measurements. Lastly, the activity profiles of GPe-TA, GPe-TI, and STN neurons demonstrate concordance with previously reported electrophysiological findings [14].

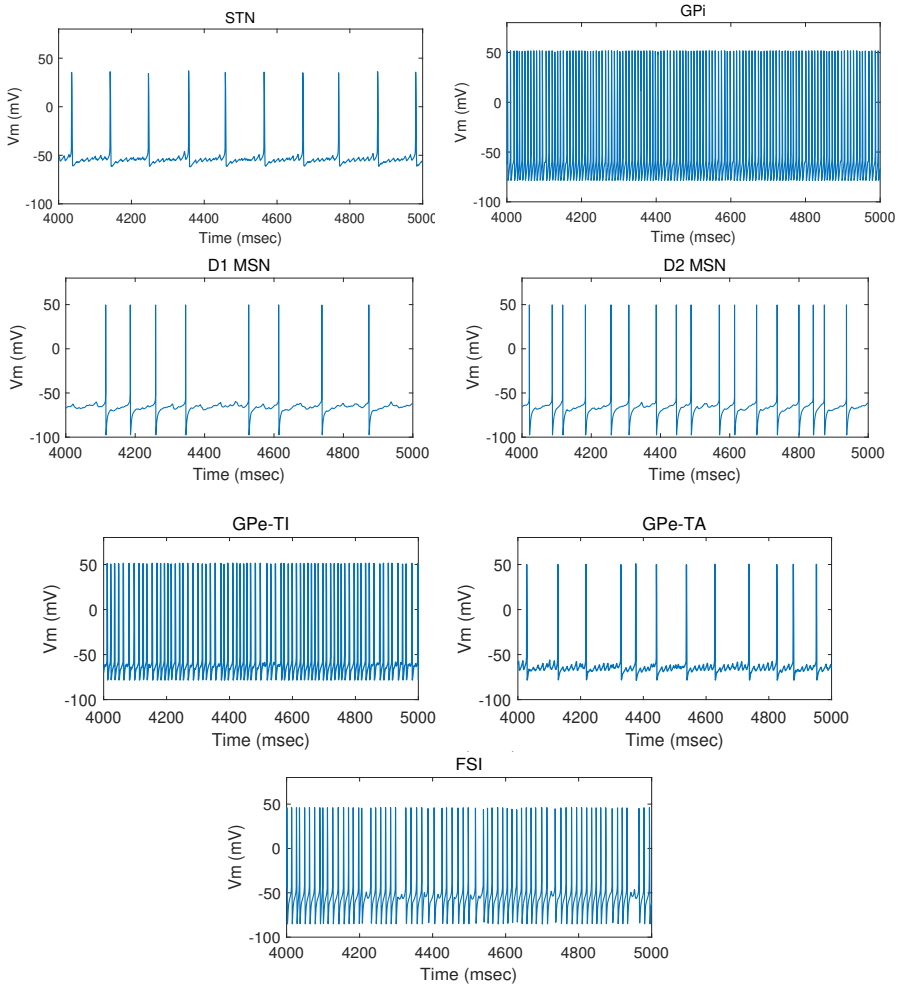

Figure 3. Representative time series of different neuronal populations under the specified model parameters in the healthy state.

Directly measuring functional synaptic connectivity among the diverse neuronal populations within the GPe remains challenging. In our model, GPe–TI (prototypical) neurons receive inhibitory input from upstream D2 MSNs and provide inhibitory outputs to STN and GPi, consistent with established descriptions of prototypical GPe circuitry. In contrast, GPe–TA (arkypallidal) neurons primarily deliver inhibitory feedback to the striatum and do not project to STN. Importantly, STN provides excitatory drive to *both* GPe–TA and GPe–TI in our connectivity scheme (Figure 1), with the effective STN→TA drive set *weaker than* STN→TI, as quantified in Table 4. These TA-specific properties (striatal feedback, absence of efferent projections to STN, and comparatively weaker STN input) follow prior experimental and modeling studies of arkypallidal neurons (e.g., [15, 17, 47–49]).

Extensive lateral connections within the GPe, as evidenced by recent physiological experiments [31], underscore the importance of local interactions in shaping the GPe's functional output. Notably, the interplay between GPe-TI and GPe-TA neurons, mediated through these local lateral connections, exhibits a marked asymmetry. GPe-TI neurons exert a robust inhibitory influence on GPe-TA neurons, a relationship that is not reciprocated equally, with the inhibitory effect from GPe-TA to GPe-TI being significantly weaker [41, 50].

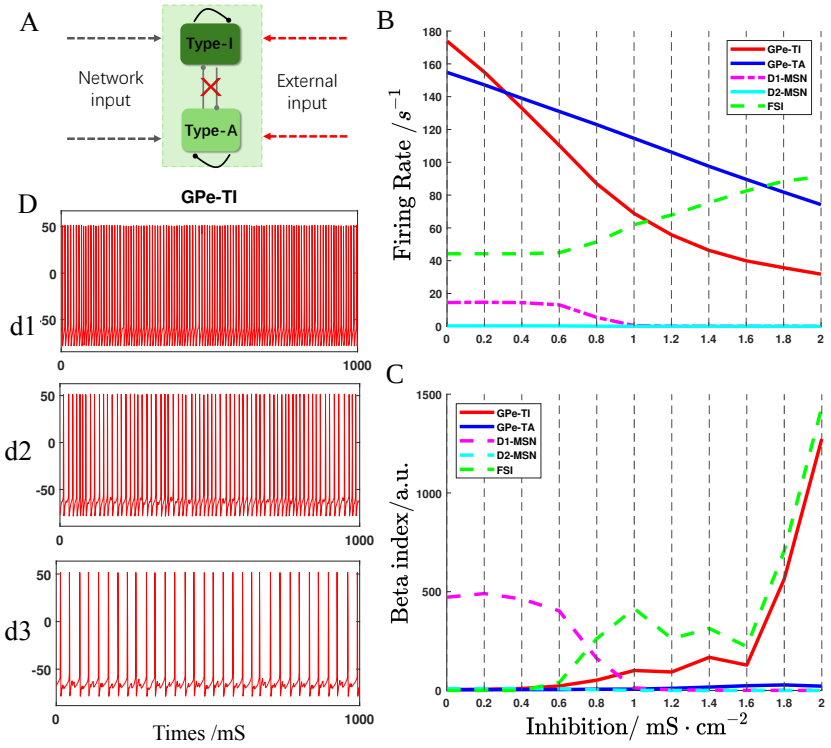

Figure 4. (**A**) Elimination of mutual inhibition connections within the heterogeneous GPe. (**B**) firing rates and (**C**) BI values obtained as the self-inhibition strength is varied from 0 mS/cm^2 up to 2 mS/cm^2. (**D**) Time series of membrane potentials for GPe-TI neurons are illustrated as the self-inhibition is adjusted to $g_{TI\to TI} = g_{TA\to TA} = 0.6$ mS/cm^2 (d1), 1 mS/cm^2 (d2), and 2.0 mS/cm^2 (d3).

This asymmetrical inhibitory interaction is essential for regulating GPe dynamics and, in turn, shaping the functional organization of the BG. The phenomenon that inhibition of GPe-TI neurons leads to diminished suppression of other GPe subtypes [46] further illustrates the complex interdependencies within the GPe network. By simulating the dynamic behaviors of GPe neurons through adjustments in the synaptic strengths of internal connections, this study seeks to illuminate the functional implications of such heterogeneity within the GPe. Specifically, we aim to investigate how variations in synaptic connection strengths affect network dynamics and the feedback mechanisms exerted on the upstream striatum. This approach would not only deepen our understanding of the intrinsic properties and functional roles of GPe neuron subtypes, but also contribute to a more comprehensive view of the BG.

3.2. Exploring the effects of mutual inhibition in heterogeneous GPe

As noted earlier, the GPe contains extensive collateral projections, giving rise to a highly interconnected network of synaptic interactions. This complexity highlights the delicate balance of inhibitory mechanisms within the GPe, an aspect that warrants deeper investigation. We therefore considered two scenarios: one in which activity is regulated only by self-inhibition, and another in which both self-inhibition and mutual inhibition jointly modulate the network dynamics. To quantify β-band (13–35 Hz) oscillations, we define the Beta Index (BI) as

$$\mathrm{BI} = \left(\int_{13}^{35} P_x(f)\,\mathrm{d}f\right) \Big/ \left(\int_{0}^{f_{\max}} P_x(f)\,\mathrm{d}f\right). \tag{3.1}$$

In the first scenario, mutual inhibition among heterogeneous GPe neurons was removed, i.e., $g_{TI\to TA} = g_{TA\to TI} = 0\,\mathrm{mS/cm^2}$, as shown in Figure 4A. Increasing the self-inhibition of TI neurons initially produced a pronounced reduction in their firing rate, which subsequently stabilized within the β-frequency range (Figure 4B). When self-inhibition exceeded $1.6\,\mathrm{mS/cm^2}$, the BI of TI neurons exhibited a notable rise, reflecting stronger oscillatory activity. In contrast, TA neurons driven only by self-inhibition and excitatory input from the STN, showed a relatively steady decline in their firing rate across conditions (Figure 4C), underscoring their distinct response relative to TI. Furthermore, the membrane potential traces of GPe-TI neurons (Figure 4D) provide a clear illustration of their transition from high-frequency discharges to more irregular, sparse spiking, thereby shifting activity into the β-band without the emergence of burst-like firing.

Simultaneously, due to feedback inhibition from the addition of GPe neurons within the model network, the firing rate of FSIs increases, along with a continuous rise in the BI value of FSI. Interestingly, in the scenario without mutual inhibition in the heterogeneous GPe, both the firing rate and BI value of D2 MSN neurons maintain at 0. The firing rate and BI value for D1 MSN neurons show initial fluctuations, but then quickly fall to zero, a consequence of inhibition exerted by FSIs onto both D1 and D2 MSN populations. Taken together, removing mutual inhibition while co-varying self-inhibition enhances FSI activity and suppresses MSN spiking, thereby attenuating transmission along the indirect pathway. This mechanism links the configuration in Figure 4 to the observed β-band enhancement in TI with all other parameters held constant.

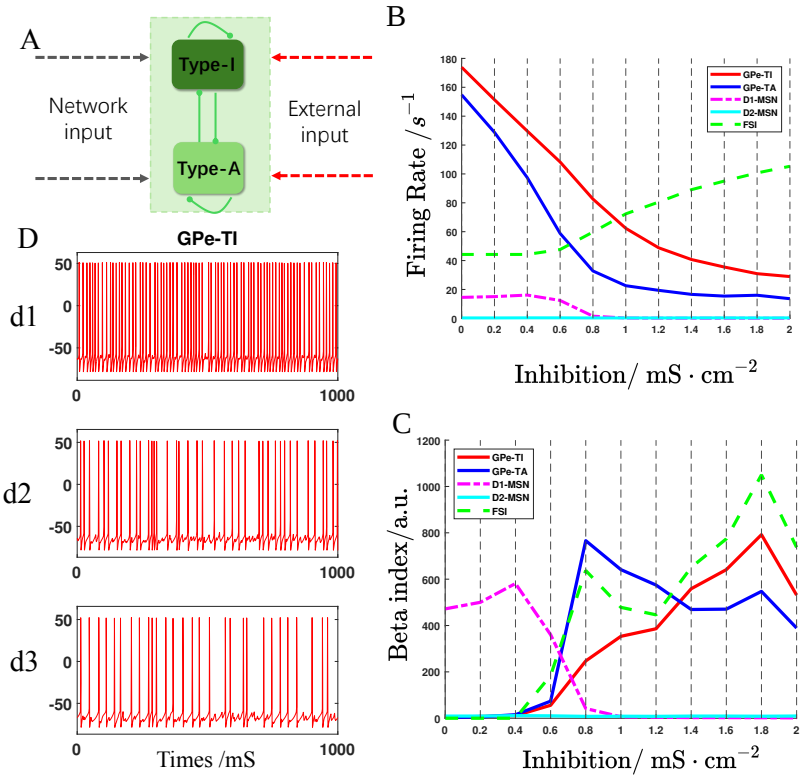

Figure 5. Influence of setting self-inhibition equivalent to mutual inhibition within the heterogeneous GPe. (**A**) illustrates the condition where all inhibitory couplings among GPe subtypes are assigned identical strengths. The corresponding firing rate plots and BI profiles, obtained as the inhibitory conductance in the GPe is gradually varied from 0 mS/cm^2 to 2 mS/cm^2, are provided in (**B**) and (**C**), respectively. (**D**) displays the membrane potential traces of GPe-TI neurons when inhibition is set to $g_{TI\to TI} = g_{TI\to TA} = g_{TA\to TI} = g_{TA\to TA} =$ 0.8 mS/cm^2 (d1), 1.4 mS/cm^2 (d2), and 1.8 mS/cm^2 (d3).

Subsequently, building upon the foundation of exclusively self-inhibition within the heterogeneous GPe, we introduce mutual inhibition to observe its effects on the network's dynamics, as illustrated in Figure 5. Considering that the number of GPe-TI neurons significantly exceeds that of GPe-TA neurons, a factor of three, and that their local axonal collaterals are considerably longer, we dismiss the possibility that mutual inhibition from TI to TA is weaker than that from TA to TI. As indicated in Figure 2, synaptic connections within this model already delineate the strengths of collateral connections; hence, we initially posit that all inhibitory connections within the GPe are equivalent, namely $g_{TI\to TI} = g_{TI\to TA} = g_{TA\to TI} = g_{TA\to TA}$. Figure 5B clearly illustrates that with progressive elevation of inhibitory synaptic conductance in the GPe, the firing activity of both TI and TA neurons decreases, eventually aligning with the β frequency band. In Figure 5C, the BI value of TA neurons tends to peak when inhibition reaches 0.8 mS/cm^2, thereafter commencing a decline, yet the firing rate remains within the β band as seen in Figure 5D, suggesting that the decrease in BI value is due to a reduction in overall power. The BI value for TI neurons reaches its maximum at 1.8 mS/cm^2, closely approximating the peak BI value observed for TA neurons. Furthermore, the introduction of mutual

inhibition within the GPe is observed to reduce the inhibition on FSIs, resulting in a higher firing rate for FSIs compared to that observed in Figure 4D, thereby maintaining the firing rate and BI value of D2 MSN neurons at zero, akin to the scenario where only self-inhibition is present within the GPe. To compare the firing patterns at certain inflection points in the BI plot, membrane potential diagrams are provided in Figure 5B, showing a gradual increase in inhibitory synaptic conductance density from top to bottom. It is observable that the spikes of TI neurons become increasingly sparse, exhibiting β band bursting activity.

3.3. Comparing the four types of inhibitory connections within the GPe

Following our discussion on the impact of the absence and presence of mutual inhibition on the firing behavior of neurons within the heterogeneous GPe (Section 3.2), this section employs a two-parameter diagram to intuitively compare the relative effects of inhibition on the network's firing dynamics. We equalize coupling within each subpopulation ($g_{TI\to TA} = g_{TA\to TI}$, $g_{TI\to TI} = g_{TA\to TA}$), and present a diagram in Figure 6, where inhibitory conductance values range from 0 mS/cm^2 to 2 mS/cm^2.

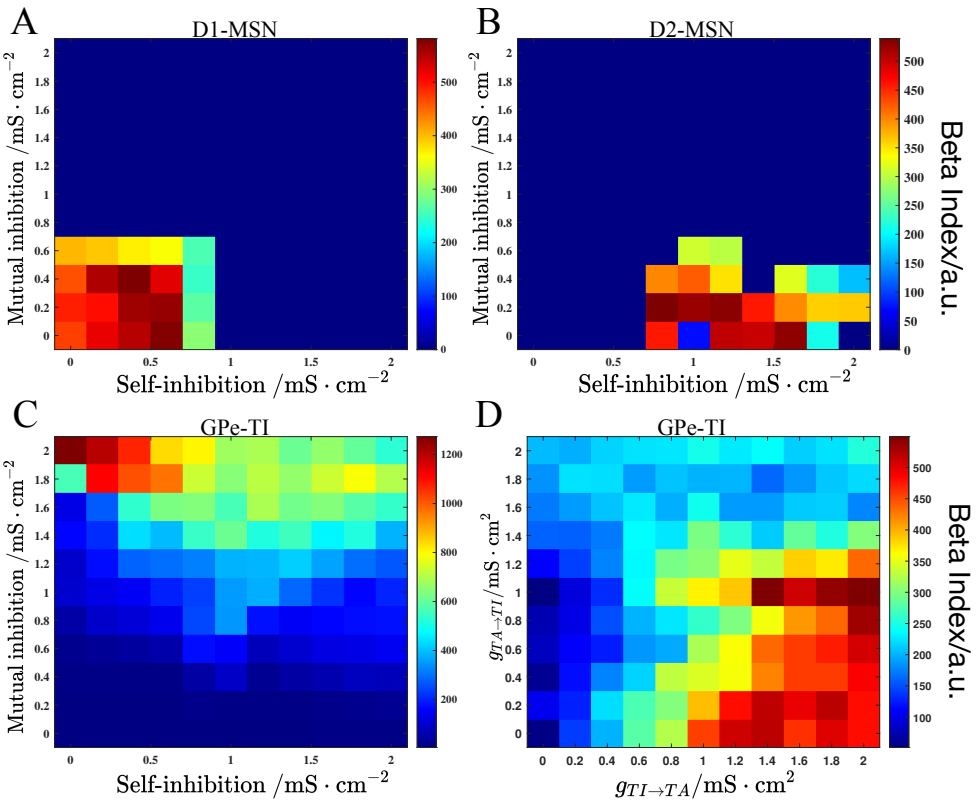

Figure 6. (**A**), (**B**), and (**C**) represent the biparametric graphs of BI values for D1 MSNs, D2 MSNs, and GPe-TI neurons, respectively, considering both self-inhibition and mutual inhibition. (**D**) illustrates the biparametric graph of BI values for GPe-TI with $g_{TI\to TI} = g_{TA\to TA} = 1$ mS/cm^2, under the joint effect of mutual inhibitory synaptic conductances $g_{TI\to TA} = g_{TA\to TI}$.

The dark blue areas in Figure 6A and 6B correspond to scenarios where the action potentials of MSN neurons are absent, indicating subthreshold oscillations under these conditions. This observation underscores the stronger influence of mutual inhibition over self-inhibition within the heterogeneous GPe. As depicted in Figure 6C, it becomes apparent that higher BI values are predominantly located above the diagonal line in the two-parameter diagram, suggesting that mutual inhibition exerts a more pronounced effect on the β-band firing behavior of GPe-TI neurons compared to self-inhibition. Additionally, it is observed that once the level of mutual inhibition reaches a threshold sufficient to induce β-band firing behavior in GPe-TI neurons, an increase in self-inhibition tends to mitigate the manifestation of this abnormal firing pattern. This nuanced interplay between self-inhibition and mutual inhibition highlights their differential contributions to regulating neuronal dynamics in the GPe, with mutual inhibition emerging as a key determinant in the generation of firing patterns within the β frequency range.

In light of the differences in self-inhibitory synaptic strengths between GPe-TI and GPe-TA neurons illustrated in Figure 2, this model simplifies the setting by assigning both parameters the same value of $1\,\mathrm{mS/cm^2}$. To further elucidate the impact of varying levels of mutual inhibition on the neural dynamics within the GPe, we maintain the self-inhibition values for both neuron subpopulations fixed at $1\,\mathrm{mS/cm^2}$. The dual-parameter heatmap in Figure 6D highlights that higher BI values are predominantly observed at elevated levels of TI to TA mutual inhibition, signifying a more substantial influence of TI-TA mutual inhibition on the network's dynamics.

The inhibitory influence originating from TI neurons is more decisive in determining their own firing characteristics than the suppression exerted by TA neurons, a result that runs counter to the initial hypothesis. Moreover, the manuscript does not present a dual-parameter comparison for MSN neurons in the context of mutual inhibition strength variations, as the action potentials for MSN neurons remain non-existent across these parameter changes. In scenarios where only self-inhibition is present within the GPe, TA neurons exhibit high-frequency firing (as shown in Figure 4D), providing sufficient inhibition to MSN neurons to prevent spike threshold breach. However, with the increase in mutual inhibition within the GPe, the inhibition from TI neurons to FSIs diminishes, leading to an elevated firing rate of FSIs which, in turn, inhibits the downstream MSN neuronal firing.

3.4. The impact of GPe feedback inhibition on the striatum

As previously mentioned, a notable innovation of the model employed here lies in the inclusion of feedback inhibition from the GPe to the striatum.

We initiate our discussion by examining the influence of the newly introduced GPe subpopulation, GPe-TA, on MSNs through its inhibitory synaptic connections, TA-D1 and TA-D2. Observations from Figure 7A reveal the impact of varying TA-D1 inhibition strength on MSNs. As TA inhibition onto D1 MSNs intensifies, their spiking activity is progressively reduced until complete silencing, while the influence on D2 MSNs is weaker and manifests as a slight increase. When the inhibitory strength from TA to D2 is varied between $0\,\mathrm{mS/cm^2}$ and $0.2\,\mathrm{mS/cm^2}$, as shown in Figure 7B, the discharge of D2 MSNs continuously decreases but does not drop to zero, unlike D1 MSNs, which only begin to exceed the firing threshold when the inhibition surpasses $0.1\,\mathrm{mS/cm^2}$. Contrary to the scenario with TA-D1 MSN inhibition, increasing TA-D2 MSN inhibition does not result in D2 MSN firing rates falling below those of D1 MSNs, thus underscoring the contrast in discharge properties of D1 versus D2 MSNs.

Furthermore, we explore the effects of eliminating inhibitory synaptic connections, TA-D1, TA-D2, TA-FSI, and TI-FSI on FSI under healthy conditions, as illustrated in Figure 7C–F. It is demonstrated that blocking the inhibitory input from TA to D1 MSNs makes FSI burst firing more pronounced, and removing the inhibitory input from TI neurons to FSIs transforms FSI firing behavior into more regular high-frequency firing. This indicates that the inhibitory connections from TA neurons to D1 MSNs have a stronger impact on FSIs than the direct inhibition from GPe to FSI neurons, presenting an intriguing conclusion about the differential influence of GPe-TA and striatal microcircuitry on FSI dynamics.

These findings clearly highlight the contrasting firing behaviors of D1 and D2 MSNs, and emphasize the important contribution of GPe-TA neurons in regulating network activity via their inhibitory feedback to the striatum. The implications of this modulation extend to the firing behavior of FSIs, indicating a hierarchical influence of GPe-TA on the BG network.

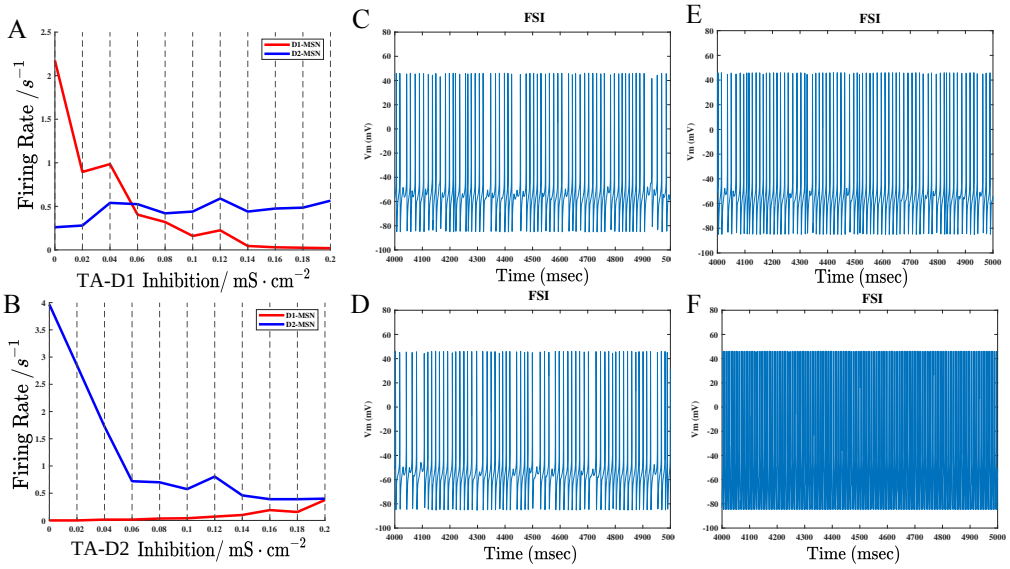

Figure 7. (**A**) and (**B**) illustrate how the firing activity of MSNs varies as the inhibitory conductance values of TA-D1 and TA-D2 connections increase from 0 mS/cm^2 to 0.2 mS/cm^2. (**C–F**) present the membrane potential traces of FSI neurons under healthy conditions when the inhibitory inputs from TA-D1, TA-D2, TA-FSI, and TI-FSI are selectively removed.

3.5. Influence of Striatal M-Current Conductance on heterogeneous GPe

Earlier investigations have suggested that interactions between the M-current and GABAergic inhibition facilitate the strengthening of β-band activity, whereas diminishing M-current conductance gives rise to pronounced β oscillations in both D1 and D2 MSNs [22]. Using our extended BG biophysical framework, we evaluated how changes in M-current conductance influence β-band activity across individual neurons. Under baseline conditions, frequency-domain analysis of GPe-TI neurons in the indirect pathway revealed no evident β oscillations (Figure 8A). For clarity, the M-current conductances of D1 and D2 MSNs are denoted as m_1 and m_2, respectively. Figure 8B illustrates that when both m_1 and m_2 are simultaneously lowered, the β-band power markedly increases as their values

drop from 2.6 mS/cm^2 to 1 mS/cm^2. These pathological rhythms within the BG appear to arise in the striatum and propagate to GPe-TI neurons. Two routes mediate this effect: one directly via reduced m_2 influencing D2 MSNs and their indirect projections to GPe-TI, and the other through decreased m_1, which first modulates collateral inhibition from D1 to D2 MSNs and subsequently reaches the TI population through the indirect pathway. To disentangle the respective contributions of m_1 and m_2, we manipulated them independently. Figure 8C shows the case of reduced m_1 (1 mS/cm^2) with normal m_2 (2.6 mS/cm^2), while Figure 8D presents the opposite condition. Compared with Figure 8C, more robust β oscillations are evident in Figure 8D, resembling the condition where both m_1 and m_2 are reduced (Figure 8B). This outcome emphasizes that inhibitory projections from D2 MSNs to GPe-TI exert stronger influence, in agreement with physiological data [33].

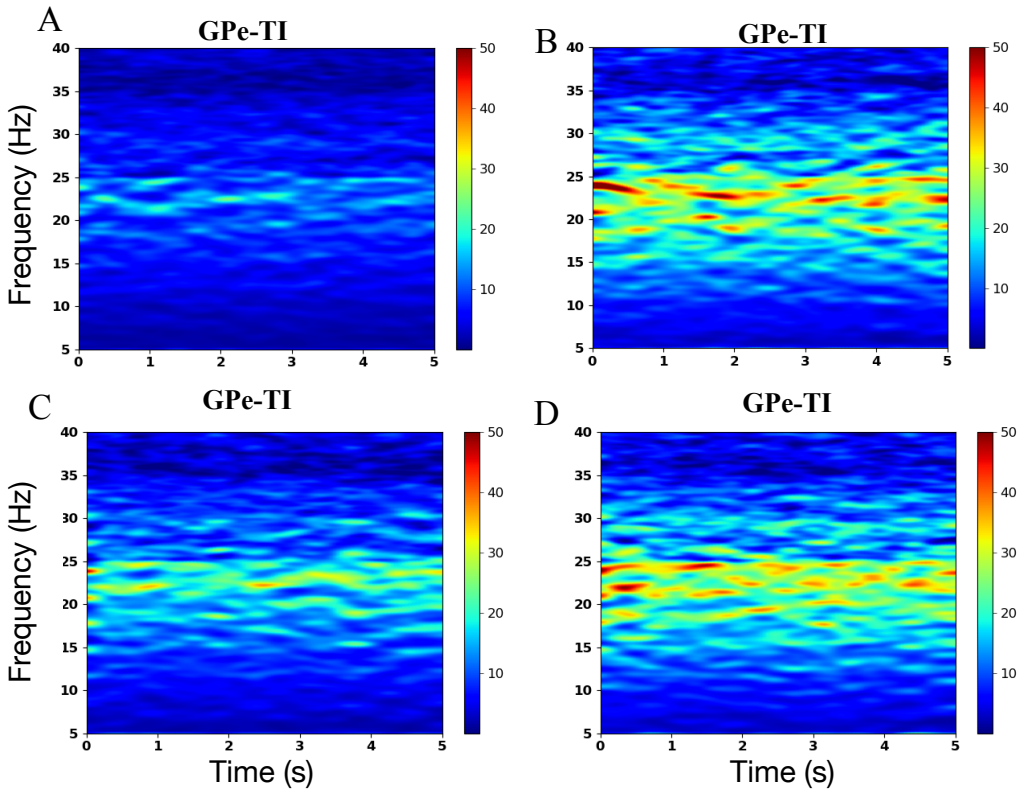

Figure 8. Spectral analysis of GPe-TI neurons across four scenarios. (**A**) Healthy state, $m_1 = m_2 = 2.6$ mS/cm^2. (**B**) Reduced M-current conductances in both D1 and D2 MSNs, $m_1 = m_2 = 1$ mS/cm^2. (**C**) Selective reduction of D1 MSN M-current, $m_1 = 1$ mS/cm^2, $m_2 = 2.6$ mS/cm^2. (**D**) Selective reduction of D2 MSN M-current, $m_1 = 2.6$ mS/cm^2, $m_2 = 1$ mS/cm^2.

3.6. Pathological states for the extended BG network model

In the PD state, the BG network exhibits pronounced β-band oscillations and increased level of synchrony [22, 33, 51]. Particularly, the loss of dopamine in the striatum leads to an increase in acetylcholine levels [33], which in turn results in a decrease in the M-type potassium currents in MSNs. To accurately replicate these changes in our model, g_M is reduced from 2.6 mS/cm^2 to 1.0 mS/cm^2 in

the simulation [33]. Additionally, the striatal output and the excitatory impacts from the STN on both GPe and GPi were increased, leading to synchronous patterns [52]. In contrast, the connections among different types of GPe neurons underwent divergent changes, while inhibitory interactions within homogeneous GPe neurons were strengthened, culminating in β-band oscillations within the GPe [53, 54]. Finally, we altered the input currents for the GPe, GPi, and STN neurons to reflect these physiological adjustments. These modifications are detailed in Table 5. For completeness, we additionally report thalamic readouts comparing healthy and PD conditions in the Appendix (Figure A2) together with the corresponding thalamic EI values (Table A1).

Table 5. Altered synaptic parameters in the PD state.

Connection	Value (mS/cm^2)	Connection	Value (mS/cm^2)
$g_{TI\to TI}$	1.5	$g_{TA\to TA}$	1.5
$g_{TI\to TA}$	0.6	$g_{TA\to TI}$	0.4
$g_{D1\to GPi}$	0.8	$g_{D2\to TI}$	0.8
$g_{STN\to TA}$	0.5	$g_{STN\to TI}$	1
$g_{STN\to GPi}$	1		
I_{GPiapp}	10	I_{STNapp}	10
$I_{GPe-TIapp}$	8	$I_{GPe-TAapp}$	7

3.7. The interplay of striatum and GPe in recovery from pathological state

Evidence from both experimental observations and computational modeling has demonstrated that dopamine loss strengthens striatal inhibition targeting the GPe [55, 56]. To represent the parkinsonian state, many modeling approaches adjust striatal output accordingly. Our previous findings demonstrated that a reduction in M-current conductance within MSNs induces β-band activity, which can propagate to GPe-TI neurons. Moreover, Yu demonstrated that when both the direct and indirect striatal pathways become more active at the same time, β-band activity in the BG is strongly elevated [56]. In line with these results, the PD condition in our framework is reproduced by lowering the M-current conductance of MSNs while simultaneously strengthening the inhibitory projections from D1 MSNs to the GPi.

Here we aim to investigate the effect of introducing a new subclass, GPe-TA, into the network, which inhibits the striatum, an upstream component in traditional models. Specifically, we examine whether the introduction of GPe-TA can still induce abnormal β oscillations in the GPe when both striatal pathways (direct and indirect) are concurrently upregulated. As shown in Figure 9A, modifying the M-current conductance of MSNs together with the inhibitory projection from D1 MSNs to the GPi gives rise to abnormal β oscillations in GPe-TI.

Furthermore, we also investigate which connection, when suppressed, enables GPe–TI neurons to recover their normal firing behavior. After systematically testing the impact of blocking different synaptic pathways, Figure 9A highlights the two connections with the most significant impact on restoring healthy dynamics: specifically, the inhibition from D2 MSNs to TI neurons and the inhibitory connection from TI to TA neurons. These interventions, as demonstrated in Figure 9B, effectively diminish pathological β-band oscillations and reinstate the main firing frequency of TI neurons to the normal range of 60–80 Hz, with the β-band power approaching zero. Blocking D2 MSN→TI

directly reduces indirect-pathway drive, whereas blocking TI→TA modulates TA feedback to the striatum and thereby indirectly relieves D2 MSN→TI influence, offering a circuit-level perspective for therapeutic intervention.

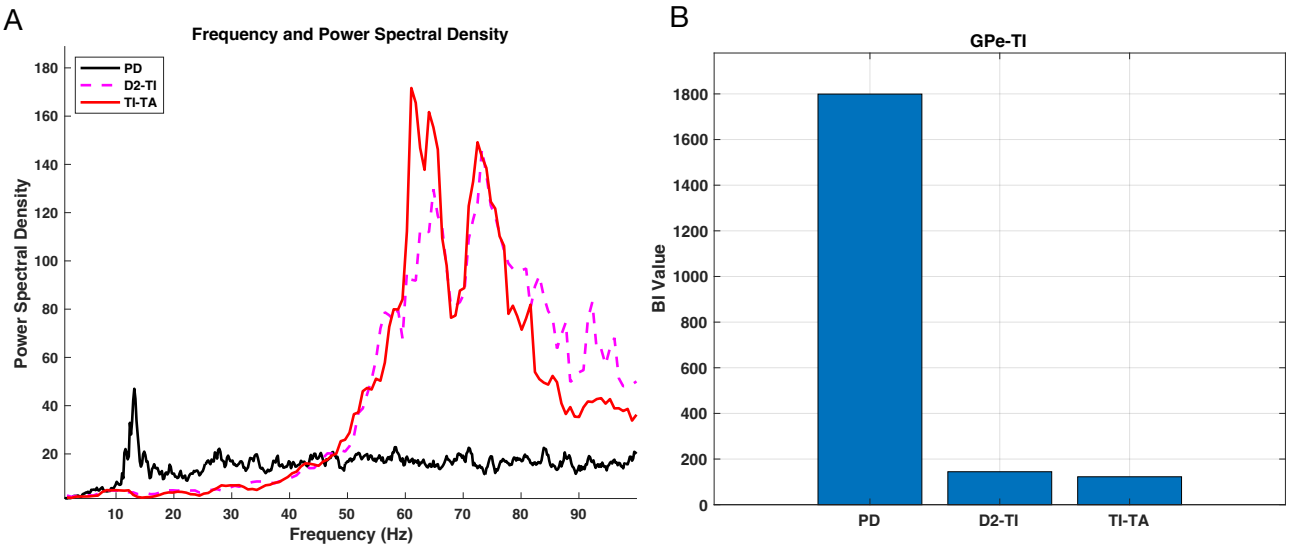

Figure 9. Changes in the power spectral density (**A**) and BI values (**B**) of GPe-TI neurons after blocking the inhibitory synaptic connection from D2 MSN to GPe-TI neurons (d2ti) and the inhibition from GPe-TI to GPe-TA neurons (tita) under PD conditions.

4. Limitations

Our model is intentionally minimal to focus on circuit mechanisms, and thus has several limitations. *(i) Simplifying assumptions.* All populations are modeled as point neurons with fixed synaptic parameters; neuromodulatory dynamics, short-term synaptic plasticity, and finer-grained within-population heterogeneity are not included. *(ii) Parameter identifiability.* Most parameters are anchored to prior studies, while a subset was tuned within literature-consistent ranges to reproduce target behaviors. For reproducibility, Tables 4 and 5 list the parameter adjustments used for the healthy and PD states. *(iii) Missing pathways.* Because the present results focus on basal ganglia circuitry, we did not explicitly model GPi efferents to thalamus in the main text. For completeness, the comparison for thalamus is provided in the Appendix (Figure A2). *(iv) External validation and scope.* Our conclusions are grounded in anatomy and physiology from prior studies and are supported by sensitivity checks within physiologically plausible ranges. Nevertheless, prospective experiments would further substantiate specific mechanism-level predictions (e.g., the relative contribution of TI–TA mutual inhibition to TI β-bursting and the effects of pallidostriatal feedback on FSI/MSN activity). We therefore present these as experimentally actionable predictions to guide future tests, rather than claims that extend beyond the model's validated domain.

5. Conclusions

We developed an extended basal ganglia model that separates arkypallidal (TA) and prototypical (TI) neurons in the external globus pallidus and incorporates the GPe→Striatum feedback pathway. This design makes two contributions that are often absent in conventional models: (i) explicit TA/TI resolution inside GPe, and (ii) pallidal feedback to the striatum. Together they allow us to examine how intra-GPe inhibition and striatal excitability jointly regulate β-band activity across nuclei.

First, under matched parameter ranges (Section 3.2; Figures 4 and 5), we show that inhibition inside GPe is a primary controller of TI β-band activity. Removing mutual inhibition and scanning self-inhibition shifts TI from high-frequency spiking to sparse β-range activity with rising BI, while TA rates decline more steadily; FSI firing rate and BI increase, and MSN spiking is differentially suppressed. Reintroducing mutual inhibition with equalized coupling strengths yields a distinct regime: both TI and TA firing rates decrease into the β band, TA exhibits a BI peak at intermediate inhibition, and TI develops robust β-bursting as inhibition grows. These results indicate that mutual inhibition is the main driver of TI β-band rhythms, whereas self-inhibition primarily limits their expression. In addition, the two-parameter maps (Figure 6) show that, across matched ranges of self- and mutual inhibition, mutual inhibition has the stronger effect on TI β-band power with a mid-range peak, whereas increasing self-inhibition primarily attenuates these rhythms.

Second, adding TA feedback to striatum exposes a strong, pathway-specific influence on MSNs and FSIs (Figure 7). Strengthening TA→D1 reduces both BI and firing rate of D1 to zero, whereas strengthening TA→D2 lowers D2 activity without silencing it; moreover, the indirect route TA→MSN→FSI affects FSI more than direct TI→FSI. Thus, the TA-mediated pallidostriatal loop shapes striatal balance and FSI activity beyond what direct pallidal inputs alone produce.

Third, manipulating striatal M-currents shows how pathology can originate upstream and propagate downstream (Figure 8). Reducing m_1/m_2 initiates β activity in striatum that then reaches TI via the indirect pathway; reducing m_2 (D2 MSNs) has a stronger effect than reducing m_1 (D1 MSNs), consistent with prior reports.

Finally, in the PD configuration (lower M-currents and strengthened D1→GPi), we identify circuit elements that restore normal TI firing (60–80 Hz) and reduce β power (Figure 9). Blocking D2→TI directly reduces indirect-pathway drive, and blocking TI→TA modulates TA feedback to striatum, indirectly relieving D2→TI influence. These pathways provide concrete, testable targets for intervention at the circuit level.

In summary, by resolving TA/TI subpopulations and including pallidostriatal feedback, the model clarifies how GPe inhibition and striatal excitability combine to generate or suppress β rhythms, and it highlights specific control points (D2→TI, TI→TA, and MSN M-currents) with practical potential for normalizing pathological dynamics. While point-neuron elements and fixed synaptic parameters were used to focus on mechanisms, extending the framework to additional GPe subclasses, neuromodulatory dynamics, and thalamocortical readouts will further increase its scope and relevance.

Author contributions statement

Zihan Li was responsible for study conception, simulations, data analysis, and manuscript writing. Xia Shi contributed to research design, experiments, data interpretation, and manuscript editing. Bei

Bai participated in experimental work and data analysis. All authors critically revised and approved the manuscript.

Use of AI tools declaration

The authors declare they have not used Artificial Intelligence (AI) tools in the creation of this article.

Acknowledgements

This work was financially supported by the National Natural Science Foundation of China under Grant No. 12272062.

Conflict of interest

The authors declare there is no conflict of interest.

References

1. G. S. Yi, J. Wang, B. Deng, X. L. Wei, Complexity of resting-state eeg activity in the patients with early-stage Parkinson's disease, *Cognit. Neurodyn.*, **11** (2017), 147–160. https://doi.org/10.1007/s11571-016-9415-z
2. L. V. Kalia, A. E. Lang, Parkinson's disease, *Lancet*, **386** (2015), 896–912. https://doi.org/10.1016/S0140-6736(14)61393-3
3. J. Jankovic, Parkinson's disease: clinical features and diagnosis, *J. Neurol. Neurosurg. Psychiatry*, **79** (2008), 368–376. https://doi.org/10.1136/jnnp.2007.131045
4. A. Cuk, T. Bezdan, L. Jovanovic, M. Antonijevic, M. Stankovic, V. Simic, et al., Tuning attention based long-short term memory neural networks for parkinson's disease detection using modified metaheuristics, *Sci. Rep.*, **14** (2024), 4309. https://doi.org/10.1038/s41598-024-54680-y
5. P. Jiang, J. R. Scarpa, V. D. Gao, M. H. Vitaterna, A. Kasarskis, F. W. Turek, Parkinson's disease is associated with dysregulations of a dopamine-modulated gene network relevant to sleep and affective neurobehaviors in the striatum, *Sci. Rep.*, **9** (2019), 4808. https://doi.org/10.1038/s41598-019-41248-4
6. M. Lindahl, I. K. Sarvestani, Ö. Ekeberg, J. H. Kotaleski, Signal enhancement in the output stage of the basal ganglia by synaptic short-term plasticity in the direct, indirect, and hyperdirect pathways, *Front. Comput. Neurosci.*, **7** (2013), 76. https://doi.org/10.3389/fncom.2013.00076
7. R. L. Albin, A. B. Young, J. B. Penney, The functional anatomy of basal ganglia disorders, *Trends Neurosci.*, **12** (1989), 366–375. https://doi.org/10.1016/0166-2236(89)90074-X
8. O. V. Popovych, P. A. Tass, Adaptive delivery of continuous and delayed feedback deep brain stimulation-a computational study, *Sci. Rep.*, **9** (2019), 10585. https://doi.org/10.1038/s41598-019-47036-4

9. V. L. Corbit, T. C. Whalen, K. T. Zitelli, S. Y. Crilly, J. E. Rubin, A. H. Gittis, Pallidostriatal projections promote β oscillations in a dopamine-depleted biophysical network model, *J. Neurosci.*, **36** (2016), 5556–5571. https://doi.org/10.1523/JNEUROSCI.0339-16.2016
10. N. Mallet, A. Pogosyan, A. Sharott, J. Csicsvari, J. Bolam, P. Brown, et al., Disrupted dopamine transmission and the emergence of exaggerated beta oscillations in subthalamic nucleus and cerebral cortex, *J. Neurosci.*, **28** (2008), 4795–4806. https://doi.org/10.1523/JNEUROSCI.0123-08.2008
11. J. Dong, S. Hawes, J. Wu, W. Le, H. Cai, Connectivity and functionality of the globus pallidus externa under normal conditions and Parkinson's disease, *Front. Neural Circuits*, **15** (2021), 645287. https://doi.org/10.3389/fncir.2021.645287
12. M. DeLong, Activity of pallidal neurons during movement, *J. Neurophysiol.*, **34** (1971), 414–427. https://doi.org/10.1152/jn.1971.34.3.414
13. R. Albin, A. Reiner, K. Anderson, L. Dure, B. Handelin, R. Balfour, et al., Preferential loss of striato-external pallidal projection neurons in presymptomatic Huntington's disease, *Ann. Neurol.*, **31** (1992), 425–430. https://doi.org/10.1002/ana.410310412
14. N. Mallet, A. Pogosyan, L. Marton, J. Bolam, P. Brown, P. Magill, Parkinsonian beta oscillations in the external globus pallidus and their relationship with subthalamic nucleus activity, *J. Neurosci.*, **28** (2008), 14245–14258. https://doi.org/10.1523/JNEUROSCI.4199-08.2008
15. N. Mallet, B. Micklem, P. Henny, M. Brown, C. Williams, J. Bolam, et al., Dichotomous organization of the external globus pallidus, *Neuron*, **74** (2012), 1075–1086. https://doi.org/10.1016/j.neuron.2012.04.027
16. Z. Abecassis, B. Berceau, P. Win, D. García, H. Xenias, Q. Cui, et al., Npas1$^{\pm}$ -nkx2.1$^{\pm}$ neurons are an integral part of the cortico-pallido-cortical loop, *J. Neurosci.*, **40** (2020), 743–768. https://doi.org/10.1523/JNEUROSCI.1199-19.2019
17. A. Abdi, N. Mallet, F. Y. Mohamed, A. Sharott, P. D. Dodson, K. C. Nakamura, et al., Prototypic and arkypallidal neurons in the dopamine-intact external globus pallidus, *J. Neurosci.*, **35** (2015), 6667–6688. https://doi.org/10.1523/JNEUROSCI.4662-14.2015
18. K. Glajch, D. Kelver, D. Hegeman, Q. Cui, H. Xenias, E. Augustine, et al., Npas1$^{\pm}$ pallidal neurons target striatal projection neurons, *J. Neurosci.*, **36** (2016), 5472–5488. https://doi.org/10.1523/JNEUROSCI.1720-15.2016
19. A. Kravitz, B. Freeze, P. Parker, K. Kay, M. Thwin, K. Deisseroth, et al., Regulation of parkinsonian motor behaviours by optogenetic control of basal ganglia circuitry, *Nature*, **466** (2010), 622–626. https://doi.org/10.1038/nature09159
20. A. C. Kreitzer, Physiology and pharmacology of striatal neurons, *Annu. Rev. Neurosci.*, **32** (2009), 127–147. https://doi.org/10.1146/annurev.neuro.051508.135422
21. A. Rădulescu, J. Herron, C. Kennedy, A. Scimemi, Global and local excitation and inhibition shape the dynamics of the cortico-striatal-thalamo-cortical pathway, *Sci. Rep.*, **7** (2017), 7608. https://doi.org/10.1038/s41598-017-07527-8

22. R. So, A. Kent, W. Grill, Relative contributions of local cell and passing fiber activation and silencing to changes in thalamic fidelity during deep brain stimulation and lesioning: a computational modeling study, *J. Comput. Neurosci.*, **32** (2012), 499–519. https://doi.org/10.1007/s10827-011-0366-4

23. D. E. Oorschot, Total number of neurons in the neostriatal, pallidal, subthalamic, and substantia nigral nuclei of the rat basal ganglia: a stereological study using the cavalieri and optical disector methods, *J. Comp. Neurol.*, **366** (1996), 580–599. https://doi.org/10.1002/(SICI)1096-9861(19960318)366:4<580::AID-CNE3>3.0.CO;2-0

24. A. H. Gittis, G. B. Hang, E. S. LaDow, L. R. Shoenfeld, B. V. Atallah, S. Finkbeiner, et al., Rapid target-specific remodeling of fast-spiking inhibitory circuits after loss of dopamine, *Neuron*, **71** (2011), 858–868. https://doi.org/10.1016/j.neuron.2011.06.035

25. T. Koós, J. M. Tepper, Inhibitory control of neostriatal projection neurons by gabaergic interneurons, *Nat. Neurosci.*, **2** (1999), 467–472. https://doi.org/10.1038/8138

26. M. Galarreta, S. Hestrin, Electrical synapses between gaba-releasing interneurons, *Nat. Rev. Neurosci.*, **2** (2001), 425–433. https://doi.org/10.1038/35077566

27. K. E. Sabol, D. B. Neill, S. A. Wages, W. H. Church, J. B. Justice, Dopamine depletion in a striatal subregion disrupts performance of a skilled motor task in the rat, *Brain Res.*, **335** (1985), 33–43. https://doi.org/10.1016/0006-8993(85)90273-2

28. K. T. Zitelli, *Cell-Type Specific Plasticity at Intrapallidal Synapses in a Mouse Model of Parkinson's Disease*, Master's thesis, University of Pittsburgh, 2016, Available from: https://core.ac.uk/download/pdf/78482375.pdf.

29. C. Miguelez, S. Morin, A. Martinez, M. Goillandeau, E. Bezard, B. Bioulac, et al., Altered pallido-pallidal synaptic transmission leads to aberrant firing of globus pallidus neurons in a rat model of Parkinson's disease, *J. Physiol.*, **590** (2012), 5861–5875. https://doi.org/10.1113/jphysiol.2012.241331

30. F. Fujiyama, T. Nakano, W. Matsuda, T. Furuta, J. Udagawa, T. Kaneko, A single-neuron tracing study of arkypallidal and prototypic neurons in healthy rats, *Brain Struct. Funct.*, **221** (2016), 4733–4740. https://doi.org/10.1007/s00429-015-1152-2

31. M. Cazorla, F. de Carvalho, M. Chohan, M. Shegda, N. Chuhma, S. Rayport, et al., Dopamine D2 receptors regulate the anatomical and functional balance of basal ganglia circuitry, *Neuron*, **81** (2014), 153–164. https://doi.org/10.1016/j.neuron.2013.10.041

32. K. J. Mastro, R. S. Bouchard, H. A. K. Holt, A. H. Gittis, Transgenic mouse lines subdivide external segment of the globus pallidus (gpe) neurons and reveal distinct gpe output pathways, *J. Neurosci.*, **34** (2014), 2087–2099. https://doi.org/10.1523/JNEUROSCI.4646-13.2014

33. M. McCarthy, C. Moore-Kochlacs, X. Gu, E. Boyden, X. Han, N. Kopell, Striatal origin of the pathologic beta oscillations in Parkinson's disease, *PNAS*, **108** (2011), 11620–11625. https://doi.org/10.1073/pnas.1107748108

34. S. Damodaran, R. C. Evans, K. T. Blackwell, Synchronized firing of fast-spiking interneurons is critical to maintain balanced firing between direct and indirect pathway neurons of the striatum, *J. Neurophysiol.*, **111** (2014), 836–848. https://doi.org/10.1152/jn.00382.2013

35. J. A. Wolf, J. T. Moyer, M. T. Lazarewicz, D. Contreras, M. Benoit-Marand, P. O'Donnell, et al., Nmda/ampa ratio impacts state transitions and entrainment to oscillations in a computational model of the nucleus accumbens medium spiny projection neuron, *J. Neurosci.*, **25** (2005), 9080–9095. https://doi.org/10.1523/JNEUROSCI.2220-05.2005

36. A. Saunders, K. Huang, B. Sabatini, Globus pallidus externus neurons expressing parvalbumin interconnect the subthalamic nucleus and striatal interneurons, *PLoS One*, **11** (2016), e0149798. https://doi.org/10.1371/journal.pone.0149798

37. V. Hernandez, D. Hegeman, Q. Cui, D. Kelver, M. Fiske, K. Glajch, et al., Parvalbumin$^{\pm}$ neurons and npas1$^{\pm}$ neurons are distinct neuron classes in the mouse external globus pallidus, *J. Neurosci.*, **35** (2015), 11830–11847. https://doi.org/10.1523/JNEUROSCI.4672-14.2015

38. M. Nomura, T. Fukai, T. Aoyagi, Synchrony of fast-spiking interneurons interconnected by gabaergic and electrical synapses, *Neural Comput.*, **15** (2003), 2179–2198. https://doi.org/10.1162/089976603322297340

39. P. Dodson, J. Larvin, J. Duffell, F. Garas, N. Doig, N. Kessaris, et al., Distinct developmental origins manifest in the specialized encoding of movement by adult neurons of the external globus pallidus, *Neuron*, **86** (2015), 501–513. https://doi.org/10.1016/j.neuron.2015.03.007

40. C. Deister, R. Dodla, D. Barraza, H. Kita, C. Wilson, Firing rate and pattern heterogeneity in the globus pallidus arise from a single neuronal population, *J. Neurophysiol.*, **109** (2013), 497–506. https://doi.org/10.1152/jn.00677.2012

41. Q. Cui, A. Pamukcu, S. Cherian, I. Chang, B. Berceau, H. Xenias, et al., Dissociable roles of pallidal neuron subtypes in regulating motor patterns, *J. Neurosci.*, **41** (2021), 4036–4059. https://doi.org/10.1523/JNEUROSCI.2210-20.2021

42. C. Gunay, J. Edgerton, D. Jaeger, Channel density distributions explain spiking variability in the globus pallidus: a combined physiology and computer simulation database approach, *J. Neurosci.*, **28** (2008), 7476–7491. https://doi.org/10.1523/JNEUROSCI.4198-07.2008

43. P. Moolchand, S. Jones, M. Frank, Biophysical and architectural mechanisms of subthalamic theta under response conflict, *J. Neurosci.*, 2022. https://doi.org/10.1101/2021.11.10.468101

44. D. Terman, J. E. Rubin, A. C. Yew, C. J. Wilson, Activity patterns in a model for the subthalamopallidal network of the basal ganglia, *J. Neurosci.*, **22** (2002), 2963–2976. https://doi.org/10.1523/JNEUROSCI.22-07-02963.2002

45. J. Bahuguna, A. Aertsen, A. Kumar, Existence and control of go/no-go decision transition threshold in the striatum, *PLoS Comput. Biol.*, **11** (2015), e1004233. https://doi.org/10.1371/journal.pcbi.1004233

46. A. Aristieta, M. Barresi, S. A. Lindi, G. Barrière, G. Courtand, B. de la Crompe, et al., A disynaptic circuit in the globus pallidus controls locomotion inhibition, *Curr. Biol.*, **31** (2021), 707–721. https://doi.org/10.1016/j.cub.2020.11.019

47. N. Mallet, R. Schmidt, D. Leventhal, F. Chen, N. Amer, T. Boraud, et al., Arkypallidal cells send a stop signal to striatum, *Neuron*, **89** (2016), 308–316. https://doi.org/10.1016/j.neuron.2015.12.017

48. A. H. Gittis, J. D. Berke, M. D. Bevan, C. S. Chan, N. Mallet, M. M. Morrow, et al., New roles for the external globus pallidus in basal ganglia circuits and behavior, *J. Neurosci.*, **34** (2014), 15178–15183. https://doi.org/10.1523/JNEUROSCI.3252-14.2014

49. M. Lindahl, J. H. Kotaleski, Untangling basal ganglia network dynamics and function: Role of dopamine depletion and inhibition investigated in a spiking network model, *eNeuro*, **3** (2016), ENEURO.0156–16.2016. https://doi.org/10.1523/ENEURO.0156-16.2016

50. M. Ketzef, G. Silberberg, Differential synaptic input to external globus pallidus neuronal subpopulations in *vivo*, *Neuron*, **109** (2021), 516–529. https://doi.org/10.1016/j.neuron.2020.11.006

51. P. Brown, Oscillatory nature of human basal ganglia activity: relationship to the pathophysiology of Parkinson's disease, *Mov. Disord.*, **18** (2003), 357–363. https://doi.org/10.1002/mds.10358

52. A. Ortone, A. A. Vergani, M. Ahmadipour, R. Mannella, A. Mazzoni, Dopamine depletion leads to pathological synchronization of distinct basal ganglia loops in the beta band, *PLoS Comput. Biol.*, **19** (2023), e1010645. https://doi.org/10.1371/journal.pcbi.1010645

53. X. Wang, Y. Yu, F. Han, Q. Wang, Beta-band bursting activity in computational model of heterogeneous external globus pallidus circuits, *Commun. Nonlinear Sci. Numer. Simul.*, **110** (2022), 106388. https://doi.org/10.1016/j.cnsns.2022.106388

54. X. Wang, Y. Yu, F. Han, Q. Wang, Dynamical mechanism of parkinsonian beta oscillation in a heterogeneous subthalamopallidal network, *Nonlinear Dyn.*, **111** (2023), 10505–10527. https://doi.org/10.1007/s11071-023-08381-2

55. M. A. J. Lourens, H. G. Meijer, T. Heida, E. Marani, S. A. van Gils, The pedunculopontine nucleus as an additional target for deep brain stimulation, *Neural Networks*, **24** (2011), 617–630. https://doi.org/10.1016/j.neunet.2011.03.007

56. Y. Yu, H. Zhang, L. Zhang, Q. Wang, Dynamical role of pedunculopntine nucleus stimulation on controlling Parkinson's disease, *Physica A*, **525** (2019), 834–848. https://doi.org/10.1016/j.physa.2019.04.016

Appendix

Overview. This supplement accompanies the main manuscript and provides materials for clarity and reproducibility: (i) the adjacency matrix corresponding to the connectivity diagram in the main text; and (ii) a thalamic (Th) comparison between healthy and PD conditions, together with the Th EI index.

Table A1. Thalamic EI index in healthy vs. PD.

Table A1. Values used to summarize excitation–inhibition balance in thalamus across conditions.

	Healthy	**PD**
EI index	0.0132	0.4030

Figure A1. Adjacency matrix derived from the main-text connectivity diagram.

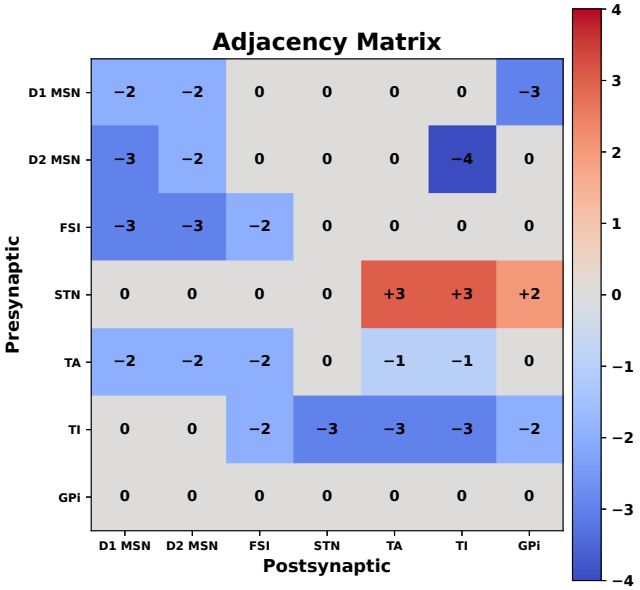

Figure A1. Cell (i, j) encodes sign $\times$ per-neuron fan-out from population i (row, presynaptic) to population j (column, postsynaptic). Abbreviations: D1/D2 MSN, FSI, STN, TA/TI (arkypallidal/prototypical GPe), GPi. Positive values denote excitatory, negative values inhibitory.

Figure A2. Thalamic (Th) activity in healthy vs. PD.

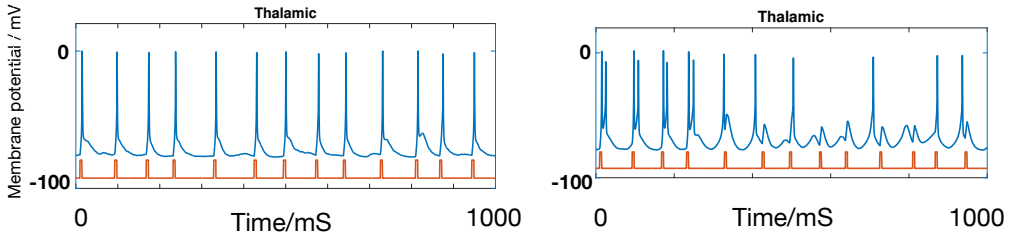

Figure A2. Side-by-side comparison of thalamic firing activity (healthy vs. PD). The corresponding Th EI indices are reported in Table A1.

AIMS Press

© 2025 the Author(s), licensee AIMS Press. This is an open access article distributed under the terms of the Creative Commons Attribution License (http://creativecommons.org/licenses/by/4.0)